

# Forces that control self-organization of chemically-propelled Janus tori

Igor Aronson (✉ [isa12@psu.edu](mailto:isa12@psu.edu))

Pennsylvania State University <https://orcid.org/0000-0002-4062-5393>

Jiyuan Wang

Heilongjiang University of Science and Technology <https://orcid.org/0000-0002-4484-0752>

Mu-Jie Huang

University of Toronto

Remmi Baker-Sediako

CELLINK Bioprinting AB

Raymond Kapral

University of Toronto <https://orcid.org/0000-0002-4652-645X>

---

## Article

### Keywords:

**Posted Date:** January 12th, 2022

**DOI:** <https://doi.org/10.21203/rs.3.rs-1096204/v1>

**License:**   This work is licensed under a Creative Commons Attribution 4.0 International License.

[Read Full License](#)

---

**Version of Record:** A version of this preprint was published at Communications Physics on July 6th, 2022. See the published version at <https://doi.org/10.1038/s42005-022-00953-9>.

# Forces that control self-organization of chemically-propelled Janus tori

Jiyuan Wang<sup>1,2</sup>, Mu-Jie Huang<sup>2</sup>, Remmi D Baker-Sediako<sup>3</sup>, Raymond Kapral<sup>2,\*</sup>, Igor S Aranson<sup>4,\*</sup>

<sup>1</sup>*School of Electrical and Control Engineering, Heilongjiang University of Science and Technology, Harbin, 150022, P. R. China*

<sup>2</sup>*Chemical Physics Theory Group, Department of Chemistry, University of Toronto, Toronto, Ontario M5S 3H6, Canada*

<sup>3</sup>*CELLINK Bioprinting AB, Arvid Wallgrens backe 20, 413 46 Göteborg, Sweden and*

<sup>4</sup>*Departments of Biomedical Engineering, Chemistry, and Mathematics, Pennsylvania State University, University Park, Pennsylvania 16802, USA*

Control of the individual and collective behavior of self-propelled synthetic micro-objects has immediate application for nanotechnology, robotics, and precision medicine. Despite significant progress in the synthesis and characterization of self-propelled Janus (two-faced) particles, predictive understanding of their behavior remains challenging, especially if the particles have anisotropic forms. Here, by using molecular simulation, we describe the interactions of chemically-propelled microtori near a wall. The results show that a torus hovers at a certain distance from the wall due to a combination of gravity and hydrodynamic flows generated by the chemical activity. Moreover, electrostatic dipolar interactions between the torus and the wall result in a spontaneous tilt and horizontal translation, in a qualitative agreement with experiment. Simulations of the dynamics of two tori near a wall provide evidence for the formation of stable self-propelled bound states. Our results illustrate that self-organization at the microscale occurs due to a combination of multiple factors, including hydrodynamic, chemical, and electrostatic interactions.

\*To whom correspondence should be addressed; E-mail: isa12@psu.edu, r.kapral@utoronto.ca

## INTRODUCTION

Individual and collective behavior of self-propelled micro-objects (also called agents or motors) is the main topic of a rapidly expanding field termed active matter [1, 2]. Recent research on synthetic active particles has demonstrated that they possess diverse functionalities which are similar to those found in the living world, such as propulsion and energy conversion [3, 4], artificial chemotaxis [5–7] and rheotaxis [8, 9], etc. However, most of the synthetic realizations of self-propelled particles lack the fidelity and efficiency of biological organisms. The limitations come mostly from micro-fabrication, resulting in relatively simple shapes such as spheres [10], rods [3], or helices [11]. These factors significantly restrict the range of possible applications of self-propelled micro-motors in robotics, drug delivery, and precision medicine [12–14].

Advances in additive manufacturing and nanoscale 3D printing allow the design of particles with practically arbitrary shape, e.g., tori or propellers [15]. Functionalization of the tori surfaces by platinum (Pt) and nickel (Ni) enables propulsion in hydrogen peroxide ( $\text{H}_2\text{O}_2$ ) solution and a response to an applied magnetic field. Without a magnetic field, the tori (with sizes between 7 and 10  $\mu\text{m}$ ) sediment and hover near the bottom wall at a distance of the order 1-2  $\mu\text{m}$ . Due to a spontaneous symmetry breaking of the hovering state, the tori tilt and translate parallel to the bottom with the speed of the order of few  $\mu\text{m}/\text{s}$ . The tori also form multiple rotating and translating bound states. If a dc magnetic field is applied

parallel to the bottom wall, the tori turn perpendicular to the bottom and swim with much higher speed (10-20  $\mu\text{m}/\text{s}$ ) in the direction controlled by the magnetic field.

In this work we use molecular simulation to uncover fundamental mechanisms governing the organization of chemically self-propelled anisotropic particles. In particular, we investigate the dynamics of Janus tori near a wall using multiparticle collision dynamics [16], a particle-based mesoscale simulation technique for complex fluids that accurately incorporates thermal fluctuations, hydrodynamic interactions, chemical reactions, and solid inclusions [17, 18]. Our results show how various interaction potentials govern the behavior of several tori interacting with each other and the confining walls. We have found that all of gravitational, hydrodynamic, and chemical interactions are responsible for the hovering behavior of a torus above the bottom wall. When the electrostatic dipolar interactions between the torus and the bottom wall are included, the torus tilts spontaneously and translates parallel to the bottom, in qualitative agreement with experiment. We also show how the interplay among the different interactions results in the formation of bound states of two tori.

## ACTIVE JANUS TORUS NEAR A WALL

The simulations of the dynamics of a torus near a wall are carried out in a system with a slab geometry: the top and bottom walls of the simulation volume are parallel to the  $(x, y)$  plane and separated by a distance  $L_z$ . Periodic boundary conditions are applied in the  $x$  and  $y$  directions with  $L_x = L_y$ . The volume contains one or more tori with centerline radius  $a$  constructed from linked overlapping spherical beads that form a ring [19]. The

torus beads are Janus spheres with catalytic  $C$  and non-catalytic  $N$  hemispherical faces. The solvent comprises  $A$  and  $B$  fluid particles. Catalytic reactions  $A \rightarrow B$  occur on the catalytic faces of the beads. Figure 1a shows a torus oriented so that the catalytic side of the torus faces the wall. The symmetry axis of the torus is indicated by the unit vector  $\hat{\mathbf{u}}$  pointing from the catalytic to noncatalytic sides of the torus. The simulation algorithm and its implementation is described in Methods.

A torus is heavier than the solvent and, due to the gravitational force  $\mathbf{F}_g$ , an inactive torus will sediment to the bottom and experience a short-range repulsive force from the wall. For an active torus where chemical reactions occur on its catalytic surface, because of the asymmetric distribution reactants  $A$  and products  $B$  a diffusiophoretic mechanism [20–22] operates to propel the torus in solution. The magnitude and direction of the diffusiophoretic force  $\mathbf{F}_d$  on the torus depends on the interactions of the reactive species with the torus beads and the displacement from equilibrium. [23] We adopt the following convention: if the diffusiophoresis force  $\mathbf{F}_d$  is in the same direction as the  $\hat{\mathbf{u}}$ -vector, i.e., towards the noncatalytic (passive) surface, it is called a backward-moving torus. If it is a direction opposite to  $\hat{\mathbf{u}}$ , it is a forward-moving torus.

If a backward-moving torus is initially oriented so that its catalytic surface faces the wall as in Fig. 1a, then the gravitational and diffusiophoretic forces will have opposite signs. Consequently, the torus will be confined to the vicinity of the wall, provided that  $F_g > F_d$ , if there are no sufficiently large orientational fluctuations allowing the torus to change its orientation relative to the wall so that escape is possible. Correspondingly, the orientation of a forward-moving torus relative to the wall must be opposite of that of a backward-moving torus for confinement to occur. Under these conditions, we can investigate the torus dynamics in the vicinity of the wall versus the strength of the confining gravitational force.

The probability distribution  $P(z)$  of the distance of the center of mass (c.o.m.) of the backward-moving torus from the wall is shown in Fig. 1b for several values of the gravitational strength parameter  $g$  (the value of  $g$  can be adjusted by the mass density of the torus material). For the  $g$  values in the range (0.1 – 0.3) presented in the figure, the torus remains confined to the vicinity of the wall and, as expected, the mean distance from the wall increases as  $g$  decreases. For  $g \lesssim 0.15$ , the torus beads do not experience direct repulsive interactions with the wall. This behavior indicates that the observed hovering is due to diffusiophoresis generated by chemical reactions rather than the short-range repulsive forces.

The tilt angle  $\theta$  of the torus with respect to the bottom plane is determined from the scalar product of their normal vectors:  $\cos(\theta) = \hat{\mathbf{u}} \cdot \hat{\mathbf{z}}$ . The probability distribution of  $\theta = \arccos(\hat{\mathbf{u}} \cdot \hat{\mathbf{z}})$ ,  $p(\theta)$ , normalized so that  $\int_0^\pi d\theta \sin \theta p(\theta) = 1$ , is shown in Fig. 1c. All distribu-

tions are peaked at the origin and broaden as  $g$  decreases, indicating larger angular fluctuations as the confinement to the wall vicinity weakens. For  $g = 0.3$ , the torus interacts strongly with the wall through short-range repulsive forces and  $p(\theta)$  (not shown) has a very narrow peak at zero.

The forms of the concentration and fluid velocity fields that accompany the diffusiophoretic mechanism provide additional insight into the origin of torus hovering. The  $c_B$  concentration and  $\mathbf{v}(\mathbf{r})$  velocity fields in the  $(x, z)$  plane near the hovering backward-moving torus with  $g = 0.15$  are shown in Fig. 2a and b. The fields are displayed in a c.o.m. reference frame. In this frame, for the concentration, we measure the average number of product  $B$  particles in a thin slab in the  $(x, z)$  plane with thickness  $\Delta = 1$  whose  $y = L/2$  coordinate lies at the torus c.o.m. The  $z$  direction in this frame is the same as the  $\hat{\mathbf{u}}$  vector of the torus. Similarly, the velocity field was calculated by averaging the velocities of all particles in volume elements with thickness  $\Delta = 1$  in the  $(x, z)$  plane. Consequently, the fields are averages over the vertical and angular displacements that the torus experiences in its motion along the wall.

As expected, Fig. 2a shows the increased product concentration in the torus hole and near the catalytic surface. In the velocity field plot (Fig. 2b) we observe that the solvent particles near the  $C - N$  interface of the torus flow from the  $N$  to  $C$  surface. We also see that there is a suction above the torus. The solvent particles flow out along the torus bottom after they flow into the hole because the wall limits the fluid flow. There are also re-circulation regions with vortices slightly above the torus. For a hovering forward-moving torus, comparison of Figs. 2c and 2a shows that the magnitude of the  $B$ -particle concentration field is significantly different because the catalytic surface no longer faces the wall. Also, comparison of the corresponding fluid velocity field near a hovering forward-moving torus surface in Fig. 2d with Fig. 2b shows that the solvent particles near the  $C - N$  interface flow from the  $C$  to  $N$  surfaces. Also, there is a suction above the torus hole that pushes the fluid particles along the torus bottom surface because the wall limits the flow.

The corresponding concentration and velocity fields for backward and forward-moving tori in the bulk fluid are shown in the middle panels of Fig. 2. Comparison of the concentration fields reveals the distortions in these fields due to the wall. The distortion of the concentration gradient affects the diffusiophoretic force and, correspondingly, the propulsion. The flow fields have a completely different form for hovering tori and those in the bulk fluid: for a backward-moving torus in the bulk phase the fluid flows outward from the noncatalytic surface of the torus and, after circulation, inward to the catalytic surface. The flow field for a cross-section of the torus is similar to that seen for a Janus colloid, as might be expected.

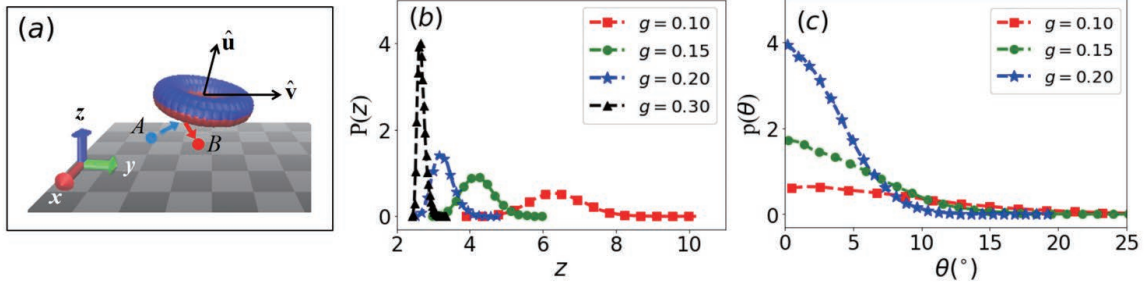


FIG. 1. (a) Janus torus with catalytic (C, red) and noncatalytic (N, blue) faces. The catalytic reaction,  $A \rightarrow B$ , occurs on the C-surface and converts fuel  $A$  particles to product  $B$  particles. The symmetry axis of the torus is indicated by the unit vector  $\hat{\mathbf{u}}$  pointing from the catalytic to noncatalytic face of the torus. The vector  $\mathbf{V}$  is the center of mass velocity. (b) The probability  $P(z)$  of the torus c.o.m.-wall distance for a backward-moving torus with its  $C$ -surface facing the wall and (c) the probability distribution  $p(\theta)$  vs  $\theta$  of a backward-moving torus for various values of gravitational strength parameter  $g$  indicated in panels (b), (c).

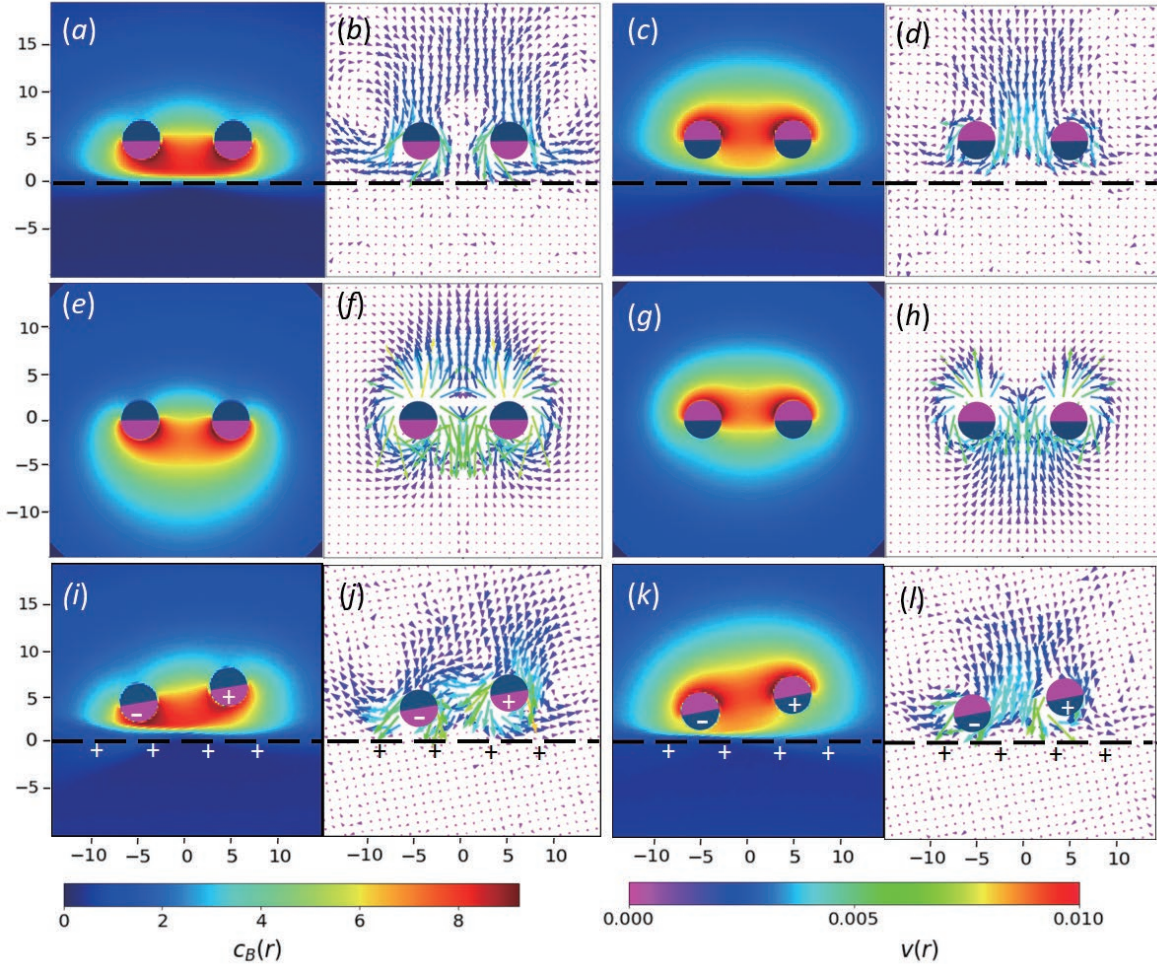


FIG. 2. Top row: (a) and (b) The  $c_B(\mathbf{r})$  concentration and  $\mathbf{v}(\mathbf{r})$  velocity fields for a hovering backward-moving torus for  $g = 0.15$ ; (c) and (d) the same fields for a hovering forward-moving torus for  $g = 0.07$ . The dashed line indicates the location of the wall at  $z = 0$ . Middle row: (e) and (f) The  $c_B(\mathbf{r})$  concentration and  $\mathbf{v}(\mathbf{r})$  velocity fields for a backward-moving torus in the bulk fluid (no gravitational force); (g) and (h) The same fields for a forward-moving torus in the bulk fluid. Bottom row: Same as top row but including the effect of charge-dipole interactions with strength  $\epsilon_{cd} = 0.2$ . The  $\pm$  symbols indicate the sign of electric charges.

The direction of the fluid velocity of the forward-moving torus is opposite to that for a backward-moving torus.

### EFFECT OF ELECTROSTATIC FORCES ON THE TORUS INTERACTION WITH THE WALL

Experimental results reported in Ref. [15] indicated that a torus acquires an electric dipolar moment resulting from the electrochemical reactions occurring on the Pt surface of a torus. This conclusion is supported by the following observation: a torus collected negatively charged  $1\ \mu\text{m}$  polystyrene spheres along its Pt surface and accumulated  $2\ \mu\text{m}$  positively charged latex spheres along its polymer surface. To incorporate this effect, we included electric dipoles with the strength  $\epsilon_{\text{cd}}$  in the model: each bead  $i$  in the torus interacts with a uniformly charged wall with through the interaction potential  $V_{\text{cd}}^{(b)}(z_i)$  in Eq. (10) in the Methods section. The potential gives rise the force  $\mathbf{F}_{\text{cd}} = -(\partial V_{\text{cd}}^{(b)}/\partial z_i)\hat{\mathbf{z}} \equiv \mathcal{F}_{\text{cd}}\gamma\hat{\mathbf{z}}$ , where  $\gamma = \cos(2\pi i/(N_b - 1))$  controls the sign and relative magnitude of the dipole of the  $N_b$  beads in the torus.

As one sees from Fig. 3a, the electrostatic interaction results in a symmetry breaking of the horizontally hovering state and the shift of  $\theta_{\text{max}}$ , the tilt angle at the maximum in  $p(\theta)$ , from  $\theta_{\text{max}} = 0$  to  $\theta_{\text{max}} > 0$ . Figure 3b plots  $\theta_{\text{max}}$  versus the charge-dipole strength  $\epsilon_{\text{cd}}$  where it is seen that beyond a critical value  $\epsilon_{\text{cd}}^* \approx 0.11$  it takes nonzero values and increases with increasing  $\epsilon_{\text{cd}}$ . This effect is also seen in the bottom panels of Fig. 2i-f that display the concentration and velocity field plots for backward and forward moving tori with charge-dipole interactions. These fields show the asymmetries that are expected in view of tilted geometries that break the symmetry of the horizontal state.

Furthermore, a tilted torus translates parallel to the bottom wall with a velocity proportional to the tilt angle  $\bar{\theta}$ . To examine this effect we consider the velocity  $\bar{V}_{\parallel}^{\text{u}}$  defined as follows: the projections of the motor velocity  $\mathbf{V}$  and orientation vector  $\theta_{\text{max}}$  onto the surface plane are  $\mathbf{V}_{\parallel} = \mathbf{V} \cdot \mathbf{1}_{\parallel}$  and  $\mathbf{u}_{\parallel} = \hat{\mathbf{u}} \cdot \mathbf{1}_{\parallel}$ , respectively, where  $\mathbf{1}_{\parallel} = \mathbf{1} - \hat{\mathbf{z}}\hat{\mathbf{z}}$  and  $\mathbf{1}$  is the unit tensor. The mean velocity can be defined as  $\bar{V}_{\parallel}^{\text{u}} = \langle \mathbf{V}_{\parallel} \cdot \hat{\mathbf{u}}_{\parallel} \rangle$ . Figure 3c shows that  $\bar{V}_{\parallel}^{\text{u}}$  remains constant for tilt angles below the bifurcation where  $\theta_{\text{max}} = 0$  and increases as  $\theta_{\text{max}}$  increases beyond the bifurcation point.

### DYNAMICS OF TWO TORI NEAR THE WALL

Next, we consider the dynamics of two interacting tori in the vicinity of the wall. The tori are subject to all the interactions in Eq. (11) as well as a short-range steric repulsion. To accommodate both tori in configurations

where they can separate sufficiently far from each other and behave independently, the size of the simulation box is increased to  $60 \times 60 \times 40$ . Periodic boundary conditions are again used in directions parallel to the walls.

For a pair of hovering backward-moving tori, Fig. 4 (top) shows the probability distributions  $P(z)$  vs their c.o.m. distances from the wall,  $z$ , trajectories of the c.o.m. of two different tori, and the probability distributions of the tilt angles  $\theta$  of two tori,  $p(\theta)$ . We observe that for both tori the  $P(z)$  distributions practically coincide. The  $\theta$  angle distributions also very closely correspond and the average tilt angles are about the same as that for a single torus under the same conditions. The trajectories show that the distances between the tori c.o.m. are concentrated between  $D = 18$  and  $28$  so that the tori do not form a long-lived bound state. The instantaneous configuration in Fig. 4 (top) shows that the tori have no tendency to form a bound state, see Supplementary Video 1.

Two forward-moving tori with  $g = 0.07$ ,  $\epsilon_{\text{cd}} = 0.2$  behave very differently as can be seen from Fig. 4 (middle). Now both the  $P(z)$  and  $p(\theta)$  distributions are distinct, and on average, one torus lies at a distance farther from the wall than the other, also the tilt angle is larger for the upper torus. Examination of the trajectories shows that the distances between the c.o.m. of two tori are concentrated between  $D = 7.5$  and  $9$ . This indicates that the two tori are stacked in a bound state since a torus has a radius  $a = 5$ . These features are evident in the instantaneous configuration in Fig. 4 (middle), see also Supplementary Video 2.

If the constant that gauges the magnitude of the gravitational force is increased to  $g = 0.09$ , the behavior of the pair of forward-moving tori changes, see Supplementary Video 3. In Fig. 4 (bottom) we see that the  $P(z)$  and  $p(\theta)$  distributions for the two tori coincide, so both tori lie at similar distances from the wall, and their tilt angles are close. In contrast to the corresponding tilt angle distribution for a single forward-moving torus,  $p(\theta)$  is peaked at the origin, and the tilt angles differ from that for a single torus near the wall. The trajectories indicate the formation of a long-lived bound state that translates and rotates. An instantaneous configuration is shown in Fig. 4 (bottom). This behavior results from stronger gravitational confinement causing the tori to adapt nearly parallel configurations to the wall. Consequently, they cannot explore regions further from the wall to adopt other configurations, such as the stacked bound state for  $g = 0.07$ .

### DISCUSSION

Here we develop a simple phenomenological theory for  $p(\theta)$ , the probability distribution of the torus tilt angle. First, we consider the system in the absence of

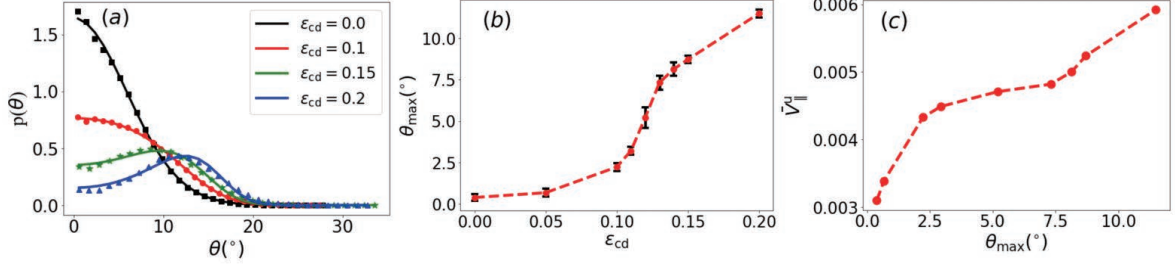


FIG. 3. (a) The probability distribution  $p(\theta)$  versus  $\theta$  for various values of  $\epsilon_{cd}$  for a backward-moving torus with  $g = 0.15$ . The symbols are the simulation data and the solid lines are fit according to Eq. (7) with fit parameters  $\gamma_1$  and  $\gamma_2$ . ( $\epsilon_{cd} : \beta\gamma_1, \gamma_2$ ): (0.0:94, 0), (0.1:1690, 0.98), (0.15:3132, 1.015), (0.2:3686, 1.024) (b) The dependence of the tilt angle  $\theta_{\max}$  versus the strength of charge-dipole interactions  $\epsilon_{cd}$ . (c) The torus velocity  $V_{\parallel}$  versus the tilt angle  $\theta_{\max}$ .

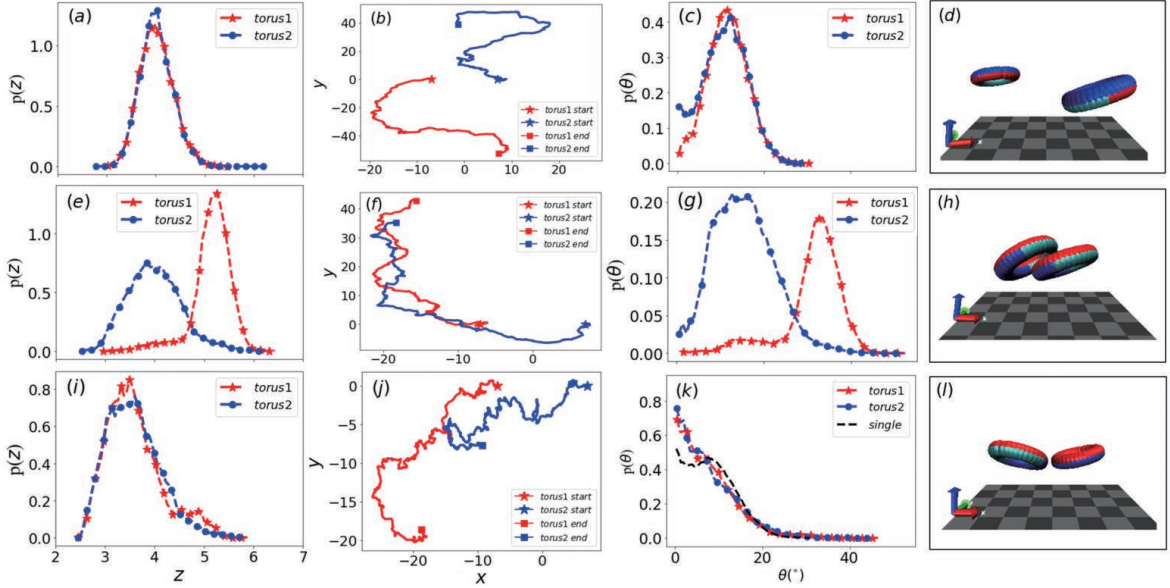


FIG. 4. (top) Backward-moving tori with  $g = 0.15$  and  $\epsilon_{cd} = 0.2$ ; (middle) forward-moving tori with  $g = 0.07$  and  $\epsilon_{cd} = 0.2$ ; (bottom) forward-moving tori with  $g = 0.09$  and  $\epsilon_{cd} = 0.2$ . The panels, left to right are: (a,e,i) the probability distribution  $P(z)$  versus  $z$ , (b,f,j) trajectories of the centers of mass of the two tori, (c,g,k) the probability distribution  $p(\theta)$  versus  $\theta$ , (d,h,l) An instantaneous configuration of the two tori.

charge-dipole interactions where the torus hovers above the wall at some distance due to hydrodynamic and diffusiophoretic forces and is subject to a gravitational force. The orientation vector of the torus is  $\hat{\mathbf{u}} = (\sin \theta \cos \phi, \sin \theta \sin \phi, \cos \theta)$ . In the Cartesian frame with  $\hat{\mathbf{z}}$  normal to the wall  $\hat{\mathbf{z}} \cdot \hat{\mathbf{u}} = \hat{u}_z = \cos \theta$  that defines the tilt angle  $\theta$ . The dynamics of the orientation vector is governed by the Langevin equation describing the dynamics of the torus,

$$\frac{d\mathbf{u}}{dt} = \zeta^{-1} \cdot (\mathbf{T}_g + \mathbf{T}_f(t)) \times \mathbf{u}. \quad (1)$$

The external torque due to the diffusiophoretic forces and gravitational field is denoted by  $\mathbf{T}_g = \gamma \mathbf{u} \times \hat{\mathbf{z}}$ , where  $\gamma$  depends on the strength of the gravitational field,  $\mathbf{T}_f$  is the fluctuating torque and  $\zeta$  is the rotational friction tensor. The Langevin equation for the dynamics of the

tilt angle can be determined from that for  $u_z$  and is given by

$$\frac{d\theta}{dt} = -\frac{\gamma}{\zeta_r} \sin \theta + \frac{1}{\zeta_r} \tilde{T}_f(t), \quad (2)$$

where the fluctuating force is  $\tilde{T}_f = T_{f,x} \sin \phi - T_{f,y} \cos \phi$  that satisfies the fluctuation-dissipation relation  $\langle \tilde{T}_f(t) \tilde{T}_f(t') \rangle = 2k_B T \zeta_r \delta(t - t')$ . Here  $\zeta_r$  is the component of the rotational friction tensor for  $u_z$  and the corresponding rotational diffusion coefficient is  $D_r = k_B T / \zeta_r$ . The Fokker-Planck equation reads

$$\partial_t p(\theta, t) = \partial_\theta \left[ \frac{\gamma}{\zeta_r} \sin \theta p \right] + D_r \partial_\theta^2 p, \quad (3)$$

whose stationary solution is

$$p(\theta) = \mathcal{N} e^{\beta \gamma \cos \theta}, \quad (4)$$

where  $\beta = 1/k_B T$  and the normalization is determined from  $\int_0^\pi d\theta \sin\theta p_s(\theta) = 1$ . This result may also be derived from Fokker-Planck equation that accounts for the effective orientational potential energy corresponding to  $u_z$ ,  $U_r(\theta) = -\gamma \cos\theta$ . The expression for  $p(\theta)$  in Eq. (4) is in accord with the simulation data in Fig. 1c and shows that the angle corresponding to the maximum in this distribution is  $\theta_{\max} = 0$ .

When the electric dipolar interaction is included the torque on the torus changes and includes another contribution  $\mathbf{T}_{cd}$ , that contributes to the previous torque and contains and additional contribution that is proportional to  $\cos\theta$ . The Langevin equation is now given by

$$\frac{d\theta}{dt} = -\frac{\gamma_1}{\zeta_r} \sin\theta(1 - \gamma_2 \cos\theta) + \frac{1}{\zeta_r} \tilde{T}_{fl}(t), \quad (5)$$

and the corresponding Fokker-Planck equation is

$$\partial_t p(\theta, t) = \partial_\theta \left[ \frac{\gamma_1}{\zeta_r} \sin\theta(1 - \gamma_2 \cos\theta) p \right] + D_r \partial_\theta^2 p, \quad (6)$$

whose stationary solution is

$$p(\theta) = \mathcal{N} e^{\beta \gamma_1 \cos\theta(1 - (\gamma_2/2) \cos\theta)}. \quad (7)$$

In this case the corresponding rotational potential energy is  $U_r(\theta) = -\gamma_1 \cos\theta(1 - (\gamma_2/2) \cos\theta)$  and has a contribution proportional to  $\cos^2\theta$  that is responsible for breaking symmetry. In contrast to the situation where there are no charge-dipole interactions, now the probability distributions indicate that the angle corresponding to the maximum in the distribution is at  $\theta_{\max} > 0$ , provided the charge-dipole strength  $\gamma_2$  is sufficiently large. Figure 3a compares the angle probability distributions  $p(\theta)$  for different values of the electric dipolar strength  $\epsilon_{cd}$  obtained from the simulations with the predictions of Eq. (7). The simulation results are in good agreement with the analytical expression in Eq. (7) showing that this simple model captures the origin of the symmetry-breaking mechanism.

## CONCLUSIONS

We have shown that a variety of forces control the behavior of chemically-propelled torus colloids near walls. They include gravitational, steric-repulsive, diffusio-phoretic, hydrodynamic, and electrostatic forces. If we neglect any of the forces, then the experimentally observed behavior cannot be reproduced. For example, no persistent horizontal translation near the wall can be obtained without electrostatic interaction. Our simulations also make a prediction that backward moving tori do not form bound states (see Fig. 4(top)). In experiment, the backward vs forward mode of propulsion is controlled by the relative thicknesses of the Pt and Ni layers [15]. For example, for thin Pt layers

(about 10 nm), the tori swim Pt (catalytic) side forward, whereas for the Pt layers thicker than 40 nm, the tori swim polymer (non-catalytic) side forward. Another important prediction from our work is that, depending on the gravitational strength, a transition from stacked bound states (Fig. 4(middle)) to flattened bound states (Fig. 4(bottom)) occurs. In turn, the effective mass density can be controlled by depositing more catalyst (PT), making the particles heavier. Alternatively, 3D printing hollow particles will make them lighter. The algorithms developed here can be applied to particles of different shapes (e.g., propellers, helices, etc.) or more complex chemical reactions. In addition to electrostatic forces, magnetic interactions can be included as well.

## METHODS

The simulation box has dimensions  $L_x = L_y = L_z = 40$  (or  $L_x = L_y = 60$  and  $L_z = 40$  for systems with two tori) and contains  $N_S = N_A + N_B$  solvent particles with mass  $m$ . The construction of the torus motor from a collection of beads was described in our earlier study of an active torus in bulk solution. [19] Here we consider tori with a centerline radius  $a = 5$  comprising  $N_b = 39$  beads with radius  $r_b$ , where neighboring beads are connected by harmonic springs with  $k_s = 500$ . The equilibrium bond length between  $i$ th and  $(i+j)$ th beads is  $r_0^{i,i+j} = 2a \sin(j\pi/N_b)$ ,  $j = 1, 2, \dots, N_b/2$ . The torus has mass  $M_{39} = 3890$ .

The  $A$  and  $B$  fluid particles undergo bounce-back collisions with the walls, and interact with each bead in a torus motor through short-range repulsive Lennard-Jones potentials. The particles interact among themselves through multiparticle collisions [16]. The torus motor interacts with the bottom wall through a short-range repulsive Lennard-Jones wall potential energy function. We also consider situations where the wall has a positive charge density and a torus has nonuniform distribution of dipoles. In this case we also have charge density-dipole interactions for each bead with the wall. To account for the effect of gravity on the motor and the possible inhomogeneous distribution of mass due to the different compositions of the catalytic and noncatalytic portions of the beads, we have a gravitational potential energy function.

More specifically, these potential energy functions have the following forms: The  $\alpha = \{A, B\}$  particles interact with the torus beads through the potential  $V_\alpha^{(b)}(r_{ki})$  with strength  $\epsilon_\alpha$ , where  $\mathbf{r}_{ki} = \mathbf{r}_k - \mathbf{r}_i$  is the vector from the center of torus bead  $i$  to fluid particle  $k$  of species  $\alpha$ . The short range potential function has the form

$$V_\alpha^{(b)}(r_{ki}) = 4\epsilon_\alpha \left[ \left( \frac{\sigma}{r_{ki} - r_b} \right)^{12} - \left( \frac{\sigma}{r_{ki} - r_b} \right)^6 + \frac{1}{4} \right], \quad (8)$$

for  $r_{ki} \leq r_c$  where  $r_c = r_b + 2^{1/6}\sigma$  and zero for  $r_{ki} > r_c$ .

We take  $\sigma = 1.0$ ,  $r_b = 1.0$ . For backward-moving tori we take  $\epsilon_A = 0.1\epsilon$ ,  $\epsilon_B = \epsilon$ , while for forward-moving tori these potential strengths are interchanged and  $\epsilon_A = \epsilon$ ,  $\epsilon_B = 0.1\epsilon$ .

Each torus bead  $i$  interacts with the bottom wall through a repulsive Lennard-Jones wall potential energy function,

$$V_w^{(b)}(z_i) = \epsilon_w \left[ \frac{1}{15} \left( \frac{\sigma_w}{z_i} \right)^9 - \frac{1}{2} \left( \frac{\sigma_w}{z_i} \right)^3 \right], \quad (z \leq z_{\min}), \quad (9)$$

and zero otherwise. Here  $z_i$  is the vertical distance of motor bead  $i$  from the lower wall at  $z = 0$ . We take  $\sigma_w = 3.0$  and  $\epsilon_w = 1.0$ . The potential is truncated at the minimum of the potential energy function at  $z_{\min} = (2/5)^{1/6} \sigma_w = 2.575$  so that the wall force vanishes for  $z \geq z_{\min}$ . A similar expression applies to the upper wall. The torus beads also interact with the bottom wall through charge density-dipole potential energy functions,

$$V_{cd}^{(b)}(z_i) = \frac{\epsilon_{cd}}{2} \ln \left( (L_z^2 + z_{ci}^2) / z_{ci}^2 \right) \cos(2\pi i / (N_b - 1)), \quad (10)$$

where each torus bead is labeled by  $i = 0, \dots, N_b - 1$  and  $z_{ci}$  is the vertical distance of motor bead  $i$  from the center of mass of the catalytic hemisphere to the bottom wall. The gravitational potential acting on a bead is given by  $V_g^{(b)}(z_{ci}) = -gz_{ci}$  where  $g$  accounts for the mass and the acceleration due to gravity.

The total interaction energy is then given by

$$V(\mathbf{r}^{N_b}, \mathbf{r}_s^{N_s}) = \sum_{i=1}^{N_b} (V_w^{(b)}(z_i) + V_{cd}^{(b)}(z_i) + V_g^{(b)}(z_i)) + \sum_{i=1}^{N_b} \sum_{\alpha=A}^B \sum_{k=1}^{N_s} \theta_k^\alpha V_\alpha^{(b)}(r_{ki}), \quad (11)$$

where  $\theta_k^\alpha$  is an indicator function that is one if particle  $k$  is species  $\alpha$  and zero otherwise.

The time evolution of the entire system is governed by molecular-dynamics-multiparticle collision dynamics. [16–18, 24] An irreversible chemical reaction,  $C + A \rightarrow C + B$ , takes place on the  $C$  hemispherical surface of each motor bead that converts species  $A$  to product  $B$ . The reactive events occur with unit probability when an  $A$  or  $B$  particle crosses a reaction radius  $R_r = r_c$ . The fluid phase reaction that is used to maintain the system in a nonequilibrium state has rate constant  $k_b = 0.001$  and is carried out using the reactive version of multiparticle collision dynamics. [25]

The molecular dynamics portion of the evolution uses the velocity-Verlet algorithm with a molecular dynamics time step,  $\delta t = 0.001$ , and the multiparticle collision dynamics portion uses a multiparticle collision time of  $\tau = 0.5$ . The collision rotation angle is  $\alpha = \pi/2$ . Grid shifting is used to insure Galilean invariance. [26] The system temperature is  $k_B T = 0.2$ . The solvent density is  $c_0 \approx 10$ , so that the approximate number of fluid particles is given by  $N_s = c_0 L_x L_y L_z$ . For  $\tau = 0.5$  the fluid

dynamic viscosity is  $\eta = 1.43$  and the common diffusion coefficient for the  $A$  and  $B$  species is  $D = 0.117$ .

Results are reported in dimensionless units with mass  $m$ , length  $\sigma$ , energy  $\epsilon$ , and time  $t_0 = \sqrt{m\sigma^2/\epsilon}$ .

## ACKNOWLEDGEMENTS

This work of R.K., J.W., and M.-J.H. was supported by a grant from the Natural Sciences and Engineering Research Council of Canada. Computations were performed on SciNet HPC Consortium computers. SciNet is funded by the Canada Foundation for Innovation through Compute Canada, the Government of Ontario, Ontario Research Excellence Fund and the University of Toronto.

The research of I.S.A. was supported by the U.S. Department of Energy, Office of Science, Basic Energy Sciences, under Award No. DE-SC0020964.

## DATA AVAILABILITY

Raw data were generated at SciNet HPC Consortium computers. Derived data supporting the findings of this study are available from the corresponding author upon reasonable request.

## AUTHOR CONTRIBUTIONS

RK and ISA designed the research, JW and MJH performed computational study, all authors discussed the results and wrote the paper.

## COMPETING INTERESTS

The Authors declare no Competing Financial or Non-Financial Interest

- 
- [1] G. Gompper, R. G. Winkler, T. Speck, A. Solon, C. Nardini, F. Peruani, H. Löwen, R. Golestanian, U. B. Kaupp, L. Alvarez, et al., “The 2020 motile active matter roadmap,” *Journal of Physics: Condensed Matter*, vol. 32, no. 19, p. 193001, 2020.
  - [2] P. Gaspard and R. Kapral, “Active matter, microreversibility, and thermodynamics,” *AAAS Research*, vol. 2020, no. 1, p. 9739231, 2020.
  - [3] W. F. Paxton, K. C. Kistler, C. C. Olmeda, A. Sen, S. K. St. Angelo, Y. Cao, T. E. Mallouk, P. E. Lamert, and V. H. Crespi, “Catalytic nanomotors: autonomous movement of striped nanorods,” *Journal of the American Chemical Society*, vol. 126, no. 41, pp. 13424–13431, 2004.

- [4] J. Wang and W. Gao, "Nano/microscale motors: biomedical opportunities and challenges," *ACS nano*, vol. 6, no. 7, pp. 5745–5751, 2012.
- [5] H. Stark, "Artificial chemotaxis of self-phoretic active colloids: Collective behavior," *Accounts of chemical research*, vol. 51, no. 11, pp. 2681–2688, 2018.
- [6] C. Jin, C. Krüger, and C. C. Maass, "Chemotaxis and autochemotaxis of self-propelling droplet swimmers," *Proceedings of the National Academy of Sciences*, vol. 114, no. 20, pp. 5089–5094, 2017.
- [7] M.-J. Huang, J. Schofield, and R. Kapral, "Chemotactic and hydrodynamic effects on collective dynamics of self-diffusiophoretic janus motors," *New J.Phys.*, vol. 19, no. 12, p. 125003, 2017.
- [8] J. Palacci, S. Sacanna, A. Abramian, J. Barral, K. Hanson, A. Y. Grosberg, D. J. Pine, and P. M. Chaikin, "Artificial rheotaxis," *Science advances*, vol. 1, no. 4, p. e1400214, 2015.
- [9] R. Baker, J. E. Kauffman, A. Laskar, O. E. Shklyaev, M. Potomkin, L. Dominguez-Rubio, H. Shum, Y. Cruz-Rivera, I. S. Aranson, A. C. Balazs, et al., "Fight the flow: the role of shear in artificial rheotaxis for individual and collective motion," *Nanoscale*, vol. 11, no. 22, pp. 10944–10951, 2019.
- [10] A. M. Pourrahimi and M. Pumera, "Multifunctional and self-propelled spherical janus nano/micromotors: Recent advances," *Nanoscale*, vol. 10, no. 35, pp. 16398–16415, 2018.
- [11] A. Ghosh and P. Fischer, "Controlled propulsion of artificial magnetic nanostructured propellers," *Nano letters*, vol. 9, no. 6, pp. 2243–2245, 2009.
- [12] W. Wang, T.-Y. Chiang, D. Velegol, and T. E. Mallouk, "Understanding the efficiency of autonomous nano-and microscale motors," *Journal of the American Chemical Society*, vol. 135, no. 28, pp. 10557–10565, 2013.
- [13] A. M. Brooks, S. Sabrina, and K. J. Bishop, "Shape-directed dynamics of active colloids powered by induced-charge electrophoresis," *Proceedings of the national academy of sciences*, vol. 115, no. 6, pp. E1090–E1099, 2018.
- [14] X. Wang, C. Hu, L. Schurz, C. De Marco, X. Chen, S. Pané, and B. J. Nelson, "Surface-chemistry-mediated control of individual magnetic helical microswimmers in a swarm," *ACS nano*, vol. 12, no. 6, pp. 6210–6217, 2018.
- [15] R. D. Baker, T. Montenegro-Johnson, A. D. Sediako, M. J. Thomson, A. Sen, E. Lauga, and I. S. Aranson, "Shape-programmed 3d printed swimming microtori for the transport of passive and active agents," *Nature communications*, vol. 10, no. 1, pp. 1–10, 2019.
- [16] A. Malevanets and R. Kapral, "Mesoscopic model for solvent dynamics," *The Journal of chemical physics*, vol. 110, no. 17, pp. 8605–8613, 1999.
- [17] R. Kapral, "Multiparticle collision dynamics: Simulation of complex systems on mesoscales," *Adv.Chem.Phys.*, vol. 140, pp. 89–146, 2008.
- [18] G. Gompper, T. Ihle, D. M. Kroll, and R. G. Winkler, "Multi-particle collision dynamics: A particle-based mesoscale simulation approach to the hydrodynamics of complex fluids," *Adv.Polym.Sci.*, vol. 221, pp. 1–87, 2009.
- [19] J. Wang, M.-J. Huang, and R. Kapral, "Self-propelled torus colloids," *The Journal of Chemical Physics*, vol. 153, no. 1, p. 014902, 2020.
- [20] J. L. Anderson, "Colloid transport by interfacial forces," *Annu. Rev. Fluid Mech.*, vol. 21, pp. 61–99, 1989.
- [21] R. Golestanian, T. B. Liverpool, and A. Ajdari, "Propulsion of a molecular machine by asymmetric distribution of reaction products," *Phys. Rev. Lett.*, vol. 94, p. 220801, 2005.
- [22] P. Gaspard and R. Kapral, "Fluctuating chemohydrodynamics and the stochastic motion of self-diffusiophoretic particles," *J.Chem.Phys.*, vol. 148, p. 134104, 2018.
- [23] P. Gaspard and R. Kapral, "Thermodynamics and statistical mechanics of chemically powered synthetic nanomotors," *Advances in Physics: X*, vol. 4, no. 1, p. 1602480, 2019.
- [24] A. Malevanets and R. Kapral, "Solute molecular dynamics in a mesoscale solvent," *The Journal of Chemical Physics*, vol. 112, no. 16, pp. 7260–7269, 2000.
- [25] K. Rohlf, S. Fraser, and R. Kapral, "Reactive multiparticle collision dynamics," *Comput. Phys. Commun.*, vol. 179, pp. 132–139, 2008.
- [26] T. Ihle and D. Kroll, "Stochastic rotation dynamics: A galilean-invariant mesoscopic model for fluid flow," *Phys. Rev. E*, vol. 63, no. 2, p. 020201, 2001.

## Supplementary Files

This is a list of supplementary files associated with this preprint. Click to download.

- [video1.mp4](#)
- [video2.mp4](#)
- [video3.mp4](#)